ChemPubSoc Europe
DOI: 10.1002/celc.201700551
CHEMELECTROCHEM
Articles

Freestanding Nanoengineered [001] Preferentially Oriented TiO_2 Nanosheets–Graphene Planarly Aligned Nanohybrids with Enhanced Li-Storage Properties

Qingwei Li,[a, c] Yuanyuan Li,[a] Lei Wang,[a] Xiaochuan Ren,[a] Jiabao Zhang,[a] Zhenhua Liao,[a] Xiang Peng,[c] Biao Gao,[b] Paul K Chu,*[c] and Kaifu Huo*[a]

A freestanding film electrode comprising face-to-face alternately stacked 2D TiO_2 nanosheets and reduced graphene oxide (rGO) is designed and fabricated as a binder-free anode for lithium-ion batteries. The ultrathin TiO_2 nanosheets, with (001) facets exposed were face-to-face hetero-assembled onto the conductive rGO, allowing Li^+ to swiftly diffuse into the TiO_2 nanosheets across the (001) facets with the lowest barrier and a short transfer distance. The configuration of this planar-aligned electrode leads to superior lithium performance, which delivers a large capacity of 132.3 $mA\,h\,g^{-1}$ with a capacity retention of 89% over 1000 cycles at a high rate of 20 C (1 C = 168 $mA\,g^{-1}$). This work proves that controlling the arrangement orientation of electrode materials with an anisotropy Li^+ diffusion barrier could remarkably improve the electrochemical properties, for promising applications in high-power energy-storage devices.

1. Introduction

The increasing market of portable devices, electrical vehicles, and grid energy storage has spurred rapid development of rechargeable lithium ion batteries (LIBs).[1–3] Anatase titanium dioxide (TiO_2) that is an effective photocatalyst in photocatalytic decomposition of organic pollutants and water splitting is also a promising anode material in LIBs due to the high operating potential relative to graphite, small volume change (3–4%) upon lithiation, low toxicity, environmental benignity, and widespread availability.[4–7] However, the low ionic diffusivity and poor electrical conductivity of TiO_2 result in low reversible capacity and limited rate performance pertaining to Li storage.[7–10] Hence, attempts have been made to overcome these hurdles and the main strategies include combining TiO_2 with conductive carbonaceous materials and fabricating nanostructured TiO_2.[10–15] For example, graphene, a typical two-dimensional (2D) carbonaceous material, is a promising host to load active materials in LIBs on account of the excellent electrical conductivity, mechanical strength, and large specific surface.[15–20] Various TiO_2/graphene composites such as nanoparticles/N-doped graphene foam,[15] electrospinning TiO_2/graphene composites[20] and mesoporous TiO_2 nanocrystals/graphene aerogels[21] possess enhanced electrochemical properties compared to pure TiO_2 due to the improved electrical conductivity of the composites.

Tuning the morphology of TiO_2 on the nanoscale is another strategy to improve the Li storage properties of TiO_2 by shortening the Li^+ diffusion distance or reducing the Li^+ diffusion barrier. It has been reported that Li^+ diffusion and electron migration across the (001) facet of anatase TiO_2 has a lower energy barrier than other crystal facets such as (101).[22–27] Thus, 2D anatase TiO_2 nanosheets with exposed (001) facet should exhibit improved reaction kinetics and rate performance in Li storage due to the larger reactive surface and lower Li^+ diffusion barrier across the (001) facet. Generally, TiO_2-based anodes are prepared by mixing 2D TiO_2 nanosheets with graphene or conductive agents as well as nonconductive organic binders followed by pressing them on the Cu foil. Thus, the 2D TiO_2 nanosheets with the exposed (001) facet are not fully parallel to the current collector in these anodes.[22,25–27] Moreover, the mass loading of TiO_2 in those anodes is generally low due to the existing of inactive materials such as binders and copper current collector. Hence, the electrochemical performance of the 2D TiO_2 is not fully utilized in these anodes. If these TiO_2 nanosheets are face-to-face hetero-assembled onto the graphene current collector to form a planarly aligned TiO_2/graphene freestanding film acting as anodes, the excellent Li storage properties such as high rate capability and large reversible capacity will be expected. For the freestanding planarly aligned TiO_2-reduced graphene oxide (rGO) hybrid electrode, since the diffusion direction of the Li^+ is in accordance with the direction of the electrostatic field that is perpendicular to the surface of the rGO current collector, Li^+ can swiftly diffuse into the TiO_2 nanosheets across the (001) facets with a low barrier and short diffusion length and the

---

[a] *Q. Li, Y. Li, L. Wang, X. Ren, J. Zhang, Z. Liao, Prof. K. Huo*
Wuhan National Laboratory for Optoelectronics (WNLO)
Huazhong University of Science and Technology
Luoyu Road, 1037, Wuhan 430074, China
E-mail: kfhuo@hust.edu.cn
[b] *Dr. B. Gao*
The State Key Laboratory of Refractories and Metallurgy
Wuhan University of Science and Technology
Wuhan 430081, China
[c] *Q. Li, X. Peng, Prof. P. K. Chu*
Department of Materials Science and Physics
City University of Hong Kong
Tat Chee Avenue, Kowloon, Hong Kong, China
E-mail: paul.chu@cityu.edu.hk

Supporting information for this article is available on the WWW under https://doi.org/10.1002/celc.201700551

electrons can transfer swiftly along the highly conductive rGO nanosheets. Such configuration of planarly aligned TiO_2-rGO paper electrode takes the advantage of 2D TiO_2 and graphene nanosheets, resulting in enhanced electrochemical properties. However, this superior hybrid film electrode has not been realized.

In this work, a freestanding film electrode comprising face-to-face alternately stacked 2D TiO_2 nanosheets and rGO is fabricated as a binder free, large-capacity, high-rate, and long cycling-life anode for LIBs. The spectacular configuration of this planarly-aligned electrode led to superior performances than other composite electrodes previously reported. The scalable fabrication process is simple and can be extended to other anode and cathode materials for LIBs.

2. Results and Discussion

The TiO_2 nanosheets with exposed (001) facets are prepared by a modified hydrothermal technique using $Ti(OC_4H_9)_4$ as the precursor.[28,29] Figure 1a depicts the field-emission scanning electron microscopy (FE-SEM) image of the hydrothermal product synthesized at 200 °C, revealing well-defined sheet-shape structures with rectangular outlines. Figures 1b and 1c present the top-view and cross-sectional transmission electron microscopy (TEM) image of the TiO_2 nanosheets which have a rectangular outline and the side length and thickness are about 200 and 10 nm, respectively. The selected-area electron diffraction (SAED) pattern (inset in Figure 1b) and high-magnification TEM (HR-TEM) image (Figure 1c) indicate that the top and bottom facets of the nanosheets are the (001) planes and the lattice spacing parallel to the top and bottom facets is about 0.235 nm, corresponding to the (001) planes of anatase TiO_2.[29] The X-ray diffraction (XRD) pattern (JCPDS No. 21-1272) and Raman scattering spectrum[15] of the nanosheets are depicted in Figure S1, which can be ascribed to anatase TiO_2. The percentage of the exposed (001) facet ratio in the anatase TiO_2 nanosheets is as large as 91 % (Figure S2).

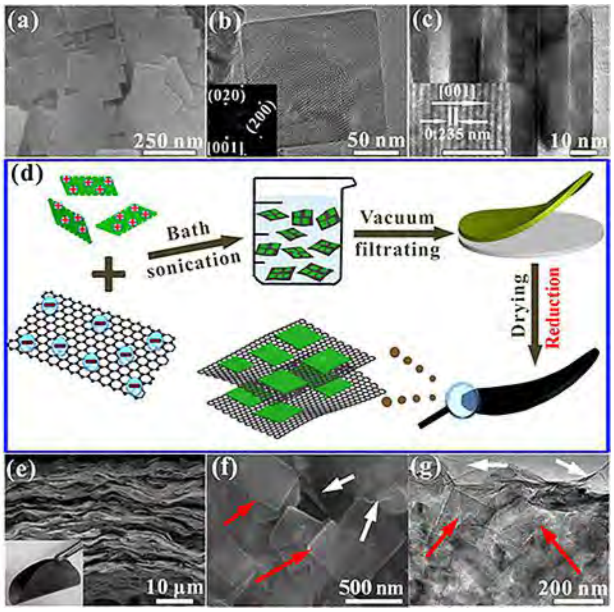

Figure 1. a) SEM image of TiO_2 nanosheets. b) TEM image of a typical TiO_2 nanosheet. c) cross-sectional TEM view of a bundle of TiO_2 nanosheets, the inset is the high-resolution TEM image of one nanosheet. d) Schematic illustration of the preparation procedures of the planarly aligned TiO_2-rGO paper electrode. The side-view SEM image (e), top-view SEM image (f), and TEM image (g) of planarly aligned TiO_2-rGO paper electrode. The red arrows indicate the TiO_2 nanosheets and the white arrows indicate the rGO. The inset digital image in (e) indicates that the paper electrode has robust flexibility.

The preparation procedures for the freestanding planarly aligned TiO_2-rGO paper electrode (denoted as planarly aligned) are schematically illustrated in Figure 1d. The TiO_2 and rGO nanosheets were prone to layer-by-layer self-assembly onto the filter membrane to afford the alternately stacked 2D TiO_2 nanosheets and rGO hybrid film[30–32] (See details in experimental section), the thickness of GO is 2.5–3 nm with the number of 8–10 layers (Figure S3). The cross-sectional SEM image (Figure 1e) discloses that the freestanding planarly aligned TiO_2-rGO paper electrode has a thickness of about 30 μm. Thermal analysis (Figure S4) reveals that the content of TiO_2 nanosheets and rGO in this film is about 93.1 wt.% and 6.9 wt.%, respectively. The digital image in the inset of Figure 1e demonstrates good flexibility and mechanical integrity of this film although it does not contain any binders. The FE-SEM image (Figure 1f) and TEM image (Figure 1g) clearly demonstrate that the thin TiO_2 nanosheets are face-to-face hetero-assembled onto the rGO nanosheets forming alternating stacked TiO_2 and rGO hybrid structure. The energy dispersive spectrometer (EDS) maps show uniform distribution of Ti, O, and C, confirming the homogeneous TiO_2-rGO hybrid structure (Figure S5). For comparison, TiO_2 nanosheets are also physically mixed with rGO to produce randomly arranged TiO_2-rGO paper electrode (denoted as randomly arranged electrode), in which some of TiO_2 nanosheets are not parallel to the rGO current collector but upright on the rGO as shown in Figure S6. Figures 2a–b are the XRD pattern and Raman spectra of planarly aligned and randomly arranged TiO_2-rGO film electrode. Although the XRD spectra demonstrate the same peak positions of anatase TiO_2 (JCPDS No. 21-1272), the intensity ratio of $I_{(004)}/I_{(101)}$ for planarly aligned TiO_2-rGO (0.69) is higher than that of randomly arranged TiO_2-rGO paper electrode (0.51). Since the upper and top and bottom faces of the nanosheets are the (001) planes and the side faces consist of

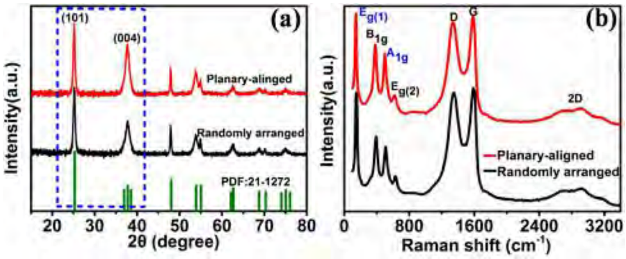

Figure 2. XRD patterns (a) and Raman spectra (b) of planarly aligned and randomly arranged TiO_2-rGO paper electrode.

(101) planes, the higher $I_{(004)}/I_{(101)}$ value suggests that more 2D TiO_2 are face-to-face assembled on the rGO forming planarly aligned TiO_2-rGO paper electrode.[33] The Raman peaks show the typical Raman shifts of anatase TiO_2[15,34] and rGO. The $E_{g(1)}$ (144 cm^{-1}) peak is ascribed to the symmetric stretching vibration of O–Ti-O of TiO_2 and the $A1_g$ (514 cm^{-1}) peak is attributed to the asymmetric bending vibration of O–Ti-O. The bonding modes on the (101) surface are the saturated Ti and O mode contributing to the symmetric stretching vibration[28] and the unsaturated Ti and O mode corresponding to asymmetric bending vibration,[34] however (001) plane comprises of the unsaturated Ti and O bonding modes. The higher intensity ratio of $I_{A1g}/I_{Eg(1)}$ for planarly aligned TiO_2-rGO (0.53) compared with randomly arranged TiO_2-rGO (0.39) means the more 2D TiO_2 are face-to-face assembled on the rGO for planarly aligned TiO_2-rGO paper electrode, which is agreement with the XRD results.

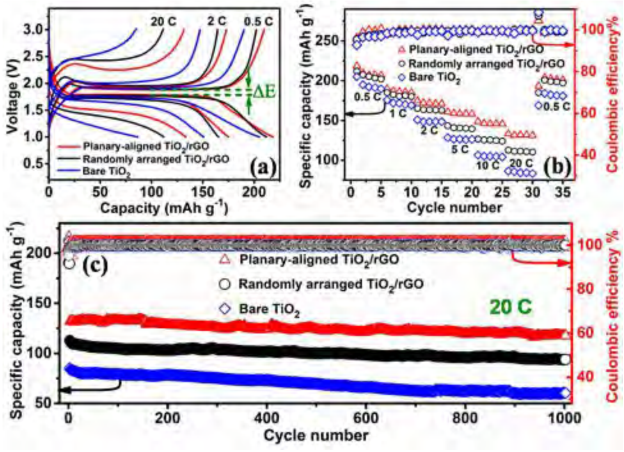

Figure 3. a) The galvanostatic charging–discharging profiles at 0.5, 2, and 20 C (1 C = 168 mA g^{-1}). b) The rate performance with coulombic efficiency. c) cycling performance and coulombic efficiency at a rate of 20 C of TiO_2 nanosheets-based electrodes.

The electrochemical properties of the TiO_2 nano-sheets based electrode are evaluated using coin-like 2025 batteries with metallic Li as the counter electrode in a voltage range of 1.0–3.0 V vs. Li^+/Li. Figure 3a displays the galvanostatic charging-discharging (GCD) profiles of the planarly aligned, randomly arranged film and bare TiO_2 nano-sheets electrodes at current rates of 0.5, 2 and 20 C (1 C = 168 mA g^{-1}). At a low rate of 0.5 C, the distinct plateaus at 1.77 and 1.90 V correspond to typical discharging (Li^+ insertion) and charging (Li^+ extraction) processes in the anatase TiO_2.[13–15] At this rate, these three electrodes deliver specific capacities of 218.5, 211.9 and 205.0 mA h g^{-1} with first coulombic efficiency of 96.0%, 95.4%, and 92.8%, respectively. The initial coulombic efficiency of our TiO_2 and TiO_2-rGO paper electrode is much higher than most other transition metal oxides, alloys and carbon based anodes.[35–37] Generally, the large initial capacity loss is a common phenomenon for metal oxide-based anodes due to the formation of unstable solid-electrolyte interphase (SEI) and poorly conductive Li_2O. The large initial coulombic efficiency of planarly aligned TiO_2-rGO electrode is mainly due to the two following reasons: (a) The TiO_2 has a high lithium ion insertion/extraction potential at about 1.70 V, which avoids the formation of unstable SEI; (b) TiO_2 stores Li via the insertion reaction mechanism, $TiO_2 + xLi^+ + xe^- \rightleftharpoons Li_xTiO_2$, while most other metal oxide anodes store Li via conversion reaction mechanism, $M_xO_y + 2yLi^+ + 2ye^- \rightleftharpoons xM + yLi_2O$ (MO_x, where M=Fe, Co, Ni, etc.), the formation of low conductive of Li_2O, causing large initial capacity loss. The large capacity of planarly aligned TiO_2-rGO film should mainly stem from TiO_2 and the capacity contribution from rGO is negligible, as depicted in Figure S7. It's worth noting that the capacity value at 0.5 C exceeds the theoretical capacity of TiO_2 (168 mA h g^{-1}) due to the large surface capacitance of nano-sized TiO_2.[15,19] The planarly aligned TiO_2-rGO hybrid film exhibits high reversibility, when the current density is further increased to 2 and 20 C, the charging and discharging plateaus of planarly aligned TiO_2-rGO hybrid film are clearly observed. ΔE is the difference between the charging and discharging potential plateaus reflecting the degree of polarization at different rates.[38] The smaller ΔE is, the better is the rate capability of the battery. As shown in Figure 3a and Figure S8, the planarly aligned TiO_2-rGO paper electrode has the lowest ΔE, especially at the high rate of 20 C. The ΔE of the planarly aligned TiO_2-rGO paper electrode is only 0.76 V, which is smaller than that of the randomly arranged TiO_2-rGO film electrode (0.94 V) and the bare TiO_2 electrode (1.21 V), implying faster Li^+ diffusion and electron transfer at the large current density. The rate capabilities of these three electrodes are presented in Figure 3b. The planarly aligned TiO_2-rGO paper showed the best rate performance, especially at high rate. At high current rates of 5, 10 and 20 C, the planarly aligned TiO_2-rGO paper electrode delivers capacities of 160.7, 148.6, and 132.3 mA h g^{-1}, respectively, which are much larger than those of the randomly arranged TiO_2-rGO paper (143.3, 126.5, 112.7 mA h g^{-1}, respectively) and bared TiO_2 (128.3, 106.4, 86.3 mA h g^{-1}, respectively). The long-term cycling stability is presented in Figure 3c. All electrodes show good cycling stability at a high rate of 20 C with high coulombic efficiency closed to 100%. However, the planarly aligned TiO_2-rGO paper electrode shows a largest capacity of 132.3 mA h g^{-1} with capacity retention of 89% over 1,000 cycles at a rate of 20 C, whereas the randomly arranged TiO_2-rGO paper delivers a capacity of 83.3 mA h g^{-1} with capacity retention of 83.3% and the bare TiO_2 delivers a capacity of 85.2 mA h g^{-1} with capacity retention of 71.0%. After 1000 cycles, the charging and discharging plateau remain intact, further indicating high reversibility (Figure S9) of the planarly aligned TiO_2-rGO paper electrode. At a low rate of 1 C, the planarly aligned TiO_2-rGO paper also shows best cycling performance than the other two electrodes (Figure S10). The superior cyclability of the planarly aligned TiO_2-rGO paper electrode should be attributed to the high electrochemical stability of TiO_2 nanosheets and hybrid electrode design by taking the advantage of 2D TiO_2 and graphene nanosheets. In the planarly aligned TiO_2-rGO free-standing hybrid film, no polymer binders and conductive additives are utilized, consequently reducing the undesirable interface,eliminating the associated overpotential and improving the utilization of active materials. Therefore, large capacity, super rate capability and prolonged cycle life are achieved for the planarly aligned TiO_2-rGO hybrid film electrode, which are superior to those previously reported TiO_2-based electrodes[14–16,19,39–48] as showed in Table 1.

Table 1. The electrochemical performances of Planarly aligned TiO_2-rGO paper electrode and other TiO_2-based electrodes.

Materials	Current density [C]	Performance [$mA\,h\,g^{-1}$]	Ref.
TiO_2/Ag hollow fibers	1	110 @ 50 cycles	[14]
Graphene/TiO_2	20	96 @ 80 cycles	[15]
TiO_2-Graphene	20	110 @ 30 cycles	[16]
TiO_2-rGO	20	108 @ 150 cycles	[19]
Self-Assembled TiO_2	4	110 @ 40 cycles	[22]
TiO_2 Hollow Spheres	20	81.4 @ 100 cycles	[39]
Carbon /TiO_2	15	29.3 @ 30 cycles	[40]
TiO_2 spheres	10	110 @ 60 cycles	[41]
Nanoporous-TiO_2	20	94 @ 70 cycles	[42]
TiO_2 Cubes	2	96 @ 30 cycles	[43]
Carbon Foams-TiO_2	12	113 @ 20 cycles	[44]
TiO_2 Mesocrystals	1	151.9 @ 60 cycles	[45]
Hierarchical TiO_2	20	99 @ 30 cycles	[46]
TiO_2 Nanosheets	10	101.9 @ 100 cycles	[47]
3D graphene/TiO_2	12	100 @ 40 cycles	[48]
Planarly aligned TiO_2-rGO paper	**1** **20**	**168 @ 400 cycles** **110 @ 1000 cycles**	**this work**

The above results clearly indicate that the rational hybrid electrode design of TiO_2 nanosheets and rGO plays an important role in the electrochemical properties. In the planarly aligned TiO_2-rGO paper electrode, rGO is used as a current collector and the (001) facets of the TiO_2 nanosheets are face-to-face assembled on the rGO and parallel to the surface of the rGO thus forming an anisotropic electrode, as schematically shown in Figure 1d and Figure 4a. Thus, Li^+ diffusing along the electric field can fully intercalate into the anatase TiO_2 across the (001) facet with a low barrier and electrons can move quickly to the TiO_2 nanosheets from the rGO thereby yielding excellent rate capability. However, if the TiO_2 nanosheets and rGO are physically mixed, some TiO_2 nanosheets are not parallel to the rGO nanosheets and even standing upright on the rGO nanosheets as schematically shown Figure 4b and Figure S6. In this case, along the direction of the electric field in LIBs, Li^+ also insert into the (101) facet during charging–discharging, thus presenting a higher barrier for Li^+ diffusion and longer diffused distance than the (001) facets.

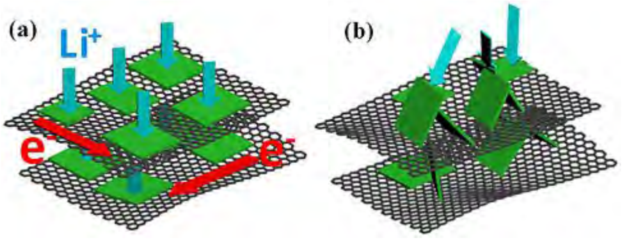

Figure 4. Schematic diagrams of lithium ion diffucion for the planarly aligned TiO_2-rGO paper electrode (a) and randomly arranged TiO_2-rGO paper electrode (b). For the planarly aligned TiO_2-rGO paper electrode in (a), Li^+ can fully intercalate into the anatase TiO_2 across the (001) facet with a low barrier and short transfer distance along the electric field.

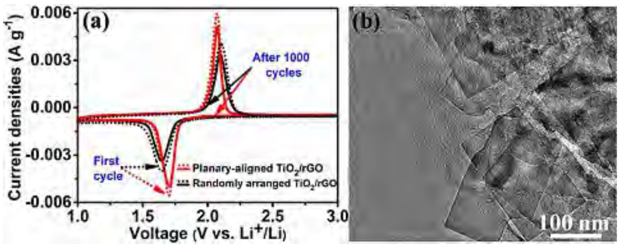

Figure 5. a) Cyclic voltammetry curves of the planarly aligned TiO_2-rGO paper electrode and randomly arranged paper electrode at the scanning rate of 0.1 $mV\,s^{-1}$ before (dot-line) and after (solid-line) 1000 cycles at the rate of 20 C. b) TEM image of the planarly aligned TiO_2-rGO paper electrode after 1000 cycles.

To further understand the improved high-rate performance and long cycle performance of the planarly aligned TiO_2-rGO paper electrode. The cyclic voltammetry profiles at a fixed scan rate of 0.1 $mV\,s^{-1}$ before and after 1000 cycles at the rate of 20 C were performed. CV curves in Figure 5a exhibit two sharp peaks at 1.7 V and 2.1 V corresponding to the Li^+ insertion/extraction reaction in anatase TiO_2, agreeing well with GCD curves in Figure 3a. The potential interval between the anodic and cathodic peaks of the planarly aligned TiO_2-rGO paper electrode is about 360 mV, which is smaller than that of the randomly arranged TiO_2-rGO film (460 mV) indicative of better rate capability. Moreover, the peak intensity of the former is larger than that of the latter,demonstrating faster Li^+ reaction kinetics and larger capacity. After 1000 cycles, the peak shapes and positions from CV curves remain the same (Figure 5), indicatinghigh stability of the paper electrode during long cycle. It also can find that after long cycle at high rate, the redox potential interval acquired from planarly aligned TiO_2-rGO paper (365 mV) is still smaller than that of the randomly arranged TiO_2-rGO film (455 mV) indicative of better rate capability of planarly aligned TiO_2-rGO paper. The morphology of the TiO_2 nanosheets has no change after 1000 cycles (Figure 5b), also revealing high structural stability of TiO_2 nanosheets.

Figure 6a and Figure S11 showed the CV curves of two different electrodes at different scanning rates. Two peaks corresponding to the Li^+ insertion/extraction reaction in anatase TiO_2 were found, agreeing well with GCD curves in Figure 3a. When the scanning rate is further increased to 1 and 2 $mV\,s^{-1}$, the charging and discharging peaks of planarly aligned TiO_2-rGO hybrid film are clearly observed, suggesting excellent chemical reversibility. ΔE can also be calculated based on the difference between the charging and discharging peaks also reflect the degree of polarization at different scan rates. The smaller ΔE is, the better rate capability of the battery is. As shown in Figure 6a and Figure S11, the ΔE became larger with the increasing scanning rate, but the accelerated speed of planarly aligned TiO_2-rGO hybrid is smaller, and the ΔE of this TiO_2-rGO electrode (0.9 V) at the high scan rate of 2 mV s^{-1} is smaller than that of the randomly arranged TiO_2-rGO film electrode (1.06 V), implying faster Li^+ diffusion and electron transfer at a large scanning rate although they have the same composition. This result is consistent with the results of GCD profiles (Figure 3a). Figure 6b illustrates the relationship between the peak current (*I*) and square root of different scanning rates in the range of 0.1–2 mV s^{-1} (details shown in Figure S11). The good linear relationship indicates that the Li insertion/extraction reaction in anatase TiO_2 in both samples is diffusion-controlled.[49] Hence, the Li^+ diffusion rate has an important effect on the Li storage properties of the hybrid electrodes. The Li^+ diffusion coefficient could be estimated according to the Randles-Sevcik equation [Eq. (1):[50]

$$I = 2.69 \times 10^5 n^{3/2} A D^{1/2} C \upsilon^{1/2} \tag{1}$$

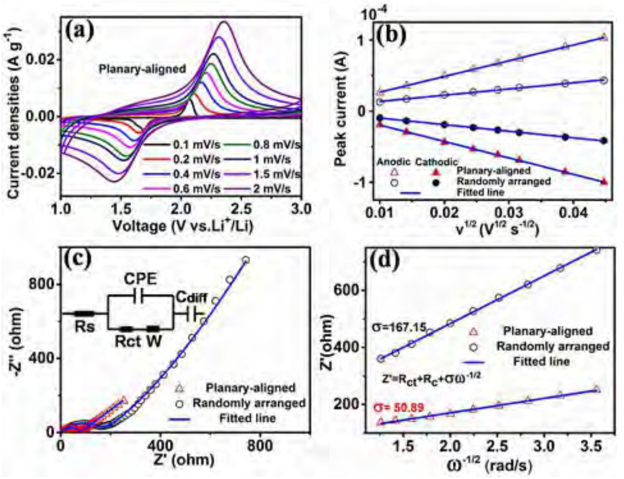

Figure 6. a) Cyclic voltammetry curves of the planarly aligned TiO_2-rGO paper at various scanning rates of 0.1, 0.2, 0.4, 0.6, 0.8, 1, 1.5, and 2 mV s^{-1}. b) Linear response of the *I* as a function of the square root of the scanning rate (ν). c) Nyquist plots and the fitted equivalent circuit. d) Linear fittings between *Z'* and the reciprocal of the square root of the angular frequency in the low-frequency region.

where n is the number of electrons in the charge transfer step (for anatase TiO_2, n = 0.5),[51] A is the surface area of the electrode (cm^2), D is the Li^+ diffusion coefficient in the different films at 298 K ($cm^2 s^{-1}$), C is the molar concentration of Li^+ in anatase TiO_2 (2.5×10^{-2} mol cm^{-3}),[51] and v is the scanning rate (V s^{-1}). The Li^+ diffusion coefficients for insertion and extraction reactions from the planarly aligned TiO_2-rGO paper are calculated to be 8.04×10^{-13} $cm^2 s^{-1}$ and 7.36×10^{-13} $cm^2 s^{-1}$, respectively, which are larger than those of the randomly arranged TiO_2-rGO paper (1.30×10^{-13} $cm^2 s^{-1}$ and 1.16×10^{-13} $cm^2 s^{-1}$), indicating faster Li^+ diffusion in the planarly aligned TiO_2-rGO hybrid paper electrode. Figure 6c shows the EIS profiles after 1000th cycle and the insets are the equivalent circuits. The electrochemical impedence spectra (EIS) of planarly aligned TiO_2-rGO hybrid before and after 1000th cycle are depicted Figure S12. The semicircle across the high-medium frequency region represents the charge transfer impedance (R_{ct}) and W represents the Warburg impedance.[49,50] After 1000th cycle, the planarly aligned TiO_2-rGO hybrid paper electrode shows a smaller R_{ct} of 69.3 Ω compared to the physically mixed paper electrode (166.6 Ω), implying higher conductivity and faster electron transport during Li^+ insertion/extraction. Moreover, the R_{ct} of the planarly aligned TiO_2-rGO hybrid paper electrode after 1000th cycle (69.3 Ω) is much smaller than that of the original electrode before cycling (410.5 Ω), indicating the better electrical contact between electrode and electrolyte due to electrolyte penetrating and activation during cycle process.[40] The inclined line in the low-frequency region of EIS corresponds to the Warburg impedance (W), which is associated with Li^+ diffusion in the electrode.[52,53] Figure 6d shows a good linear relationship between the real impedance (*Z'*) and reciprocal of the square root of the angular frequency ($\omega^{-1/2}$) in the low frequency region. The Warburg impedance coefficient (σ_w) can be obtained from the slope of *Z'* vs. $\omega^{-1/2}$ in the Warburg region and the square of σ_w is inversely proportional to the Li^+ diffusion coefficient (D_{Li^+}), that is $D_{Li^+} \propto 1/\sigma^2$ (see the Supporting Information).[52] The calculated D_{Li^+} value of lithiation in the planarly aligned TiO_2-rGO hybrid paper is about 2.89×10^{-13} $cm^2 s^{-1}$ which is one order of magnitude larger than that of the physically mixed paper of 2.68×10^{-14} $cm^2 s^{-1}$. The larger D_{Li^+} and smaller R_{ct} of the planarly aligned TiO_2-rGO hybrid paper electrode implied faster Li^+ and electron transfer, consequently resulting in higher power performance, larger capacity, and better cycling stability. The larger Li^+ diffusion coefficient in the planarly aligned TiO_2-rGO hybrid paper electrode is attributed to the special design in which the ultrathin TiO_2 nanosheets with large exposed (001) facets are face-to-face hetero-assembled onto the rGO current collector to ensure Li^+ diffusion along the [001] direction of the TiO_2 thereby yielding excellent rate capability. This layer-by-layer electrode design can be extended to prepare other analogous types of electrodes for high-power LIB and SIBs.[54]

3. Conclusions

In summary, [001] preferentially-oriented 2D TiO_2-rGO nanosheets planarly aligned paper electrodes are designed and fabricated as binder-free, large-capacity, high-rate, and long cycling-life anodes in LIBs. In such spectacular configuration of this planarly aligned electrode, the ultrathin and (001) facets exposed TiO_2 nanosheets are face-to-faced hetero-assembled onto rGO and the Li^+ diffuse along the electric field direction can fully intercalate into the (001) facets of anatase TiO_2 with a low barrier and short transfer distance. At the same time, electrons move quickly along the rGO nanosheets. The planarly aligned TiO_2-rGO hybrid paper electrode shows a high specific capacity of 132.3 mA h g^{-1} with 89% capacity retention over

1,000 cycles at a large current density of 20 C. It exhibits excellent rate capability with 63 % retention when the current density is increased 40 times from 0.5 to 20 C. This layer-by-layer electrode design by coupling different 2D materials with strong synergic effect can be extended to prepare other analogous types of electrode materials for high-power LIBs.

Experimental Section

Synthesis of TiO_2 Nanosheets

TiO_2 nanosheets with exposed (001) facets were prepared by a modified hydrothermal route.[28,29] In a typical synthesis, tetrabutyl titanate [$Ti(OC_4H_9)_4$, 12 mL] and hydrofluoric acid solution (3 mL, 50 wt.%) were mixed and then transferred in a 40 mL Teflon-lined autoclave for reaction of 24 h at 200 °C. The as-synthesized TiO_2 nanosheets were rinsed with 0.5 M NaOH solution and deionized water for several times and finally dried overnight in a vacuum oven at 80 °C.

Synthesis of Freestanding TiO_2-rGO Planar Paper Electrodes

The GO nanosheets are purchased from Sixth Elements Hi-tech Development Co. Ltd, Changzhou, China. The freestanding TiO_2-rGO planarly aligned paper electrodes were prepared similar to our previous reports.[30–32] In a typical synthesis, the as-prepared TiO_2 nanosheets were dispersed into the poly (diallyldimethylammonium chloride) (PDDA) solution under stirring to be positively charged by the absorption of PDDA cations. The GO solution with a concentration of 2 mg mL^{-1} was prepared by probe sonicating as-received GO powders. For the preparation of freestanding TiO_2-rGO planarly aligned hybrid electrodes, the positively charged TiO_2-PDDA nanosheets suspension was dropwise added into negatively-charged GO solution dispersion under ultrasonication and then vacuum-filtered through a filter membrane (220 nm pore size). The TiO_2 and GO nanosheets were prone to layer-by-layer self-assembly onto the filter membrane to afford a hybrid film. After freeze drying overnight, the freestanding film of planarly aligned TiO_2 and GO nanosheets was peeled off from the filtration membrane, followed by heating under Ar in a tube furnace at 400 °C for 3 h. During thermal treatment, the GO is reduced to form rGO nanosheets via removing hydroxy groups. Finally, freestanding superlattice-like TiO_2-rGO planarly aligned paper electrode was produced. For comparison, we also prepared the randomly arranged TiO_2-rGO electrode by physical mixing TiO_2 and GO nanosheets, vacuum filtration and following thermal treatment in Ar at 400 °C for 3 h. The bare TiO_2 electrode was prepared by mixing theTiO_2 nanosheets, carbon black and poly(vinyl difluoride) (PVDF) at a weight ratio of 80:10:10 and pasted on pure Cu foil.

Materials Characterization

The morphology, microstructure and composition of the as-synthesized products were characterized by field emission scanning electron microscopy (FE-SEM, FEI Nova 450 Nano), transmission electron microscopy (HR-TEM, FEI Titan G2 60-300) attached with X-ray energy dispersion spectrum (EDS), X-ray diffraction measurement (Philips X′ Pert Pro, Cu Kα radiation, ($\lambda = 1.5418$ Å) and Raman spectrum (HR RAMLab). The thermal analysis was performed on a thermogravimetric analysis (TGA, NETZSCH; TG 209 F3) under Ar/O_2 (10 % O_2) atmosphere with the heating rate of 10 °C/min.

Electrochemical Measurements

The electrochemical properties of the products were studied using 2025 coin cells. The electrolyte was a 1 M solution of $LiPF_6$ in a 1:1 vol/vol mixture of ethylene carbonate (EC) and diethyl carbonate (DEC). A Celgard 2400 film was used as the separator and pure Li foil as the counter electrode. The galvanostatic charging–discharging (GCD) measurement of the batteries were conducted in a potential range of 1–3 V vs. Li/Li$^+$. The specific capacity was calculated based on the mass loading of TiO_2 nanosheets in the electrode. Cyclic voltammetry (CV) was conducted on the CHI 660e electrochemical workstation and the electrochemical impedance spectra (EIS) were acquired before and after cycling 1000 at fully charged state at the rate 20 C via a Princeton applied research (Parstat4000) between 10 mHz and 10^5 Hz.

Acknowledgements

This work was financially supported by National Natural Science Foundation of China (No. 51572100, 52504171 and 61434001), Natural Science Foundation of Hubei Province (2015CFA116), HUST Key Interdisciplinary Team Project (2016JCTD101), Fundamental Research Funds for the Central Universities (HUST: 2015QN071), Outstanding Young and Middle-aged Scientific Innovation Team of Colleges and Universities of Hubei Province (T201402), and City University of Hong Kong Applied Research Grant (ARG) No. 9667122. The authors also acknowledge the Nanodevices and Characterization Centre of WNLO-HUST and Analytical and Testing Center of HUST.

Conflict of Interest

The authors declare no conflict of interest.

Keywords: freestanding film electrodes · titanium dioxide · high-rate capability · diffusion coefficient · lithium-ion batteries

[1] H. Li, Z. Wang, L. Chen, *Adv. Mater.* **2009**, *21*, 4593–4607.
[2] V. Etacheri, R. Marom, R. Elazari, G. Salitra, D. Aurbach, *Energy. Environ. Sci.* **2011**, *4*, 3243–3262.
[3] N. Kyeremateng, *ChemElectroChem*. **2014**, *1*, 1442–1466.
[4] D. Deng, M. Kim, J. Lee, J. Cho, *Energy. Environ. Sci.* **2009**, *2*, 818–837.
[5] Y. Cheng, Z. Chen, H. Wu, M. Zhu, Y. Lu, *Adv. Funct. Mater.* **2016**, *26*, 1338–1346.
[6] Z. Chen, I. Belharouak, Y. Sun, K. Amine, *Adv. Funct. Mater.* **2013**, *23*, 959–969.
[7] H. Kim, D. Mhamane, M. Kim, H. Roh, V. Aravindan, S. Madhavi, K. Roh, K. Kim, *J. Power Sources.* **2016**, *327*, 171–177.
[8] Z. Jin, ; M. Yang, J. Wang, H. Gao, Y. Lu, G. Wang, *Chem. Eur. J.* **2016**, *22*, 6031–6036.
[9] L. Zuniga, V. Agubra, D. Flores, H. Campos, J. Villareal, M. Alcoutlabi, *J Alloy Compd.* **2016**, 686, 733–743.
[10] R. Wu, S. Shen, G. Xia, F. Zhu, C. Lastoskie, J. Zhang, *ACS Appl. Mater. Interfaces.* **2016**, *8*, 19968–19978.
[11] W. Wang, Q. Sa, J. Chen, Y. Wang, H. Jung, Y. Yin, *ACS Appl. Mater. Interfaces.* **2013**, *5*, 6478–6483.
[12] B. Hao, Y. Yan, X. Wang, G. Chen, *ACS Appl. Mater. Interfaces.* **2013**, *5*, 6285–6291.
[13] B. Guan, L. Yu, J. Li, X. Lou, *Sci. Adv.* **2016**, *2*, 1–8.
[14] T. Yuan, B. Zhao, R. Cai, Y. Zhou, Z. Shao, *J. Mater. Chem.* **2011**, *21*, 15041–15048.

[15] X. Jiang, X. Yang, Y. Zhu, H. Jiang, Y. Yao, P. Zhao, C. Li, *J. Mater. Chem. A.* **2014**, *2*, 11124–11133.
[16] D. Wang, D. Cho, J. Li, Z. Yang, Z. Nie, R. Kou, D. Hu, C. Wang, L. Saraf, J. Zhang, I. Aksay, J. Liu, *ACS Nano.* **2009**, *3*, 907–914.
[17] N. Li, G. Liu, C. Zhen, F. Li, L. Zhang, H. Cheng, *Adv. Funct. Mater.* **2011**, *21*, 1717–1722.
[18] J. Chen, Z. Wang, X. Dong, P. Chen, X. Lou, *Nanoscale.* **2011**, *3*, 2158–2161.
[19] S. Yang, X. Feng, K. Müllen, *Adv. Mater.* **2011**, *23*, 3575–3579.
[20] X. Zhang, P.Suresh Kumar, V. Aravindan, H. Liu, J. Sundaramurthy, S. Mhaisalkar, H. Duong, S. Ramakrishna, S. Madhavi, *J. Phys. Chem. C.* **2012**, *116*, 14780–14788.
[21] B. Qiu, M. Xing, J. Zhang, *J. Am. Chem. Soc.* **2014**, *136*, 5852–5855.
[22] L. Nguyen, V. Aravindan, S. Kulkarni, F. Yanan, R. Prabhakar, S. Batabyal, S. Madhavi, *ChemElectroChem.* **2014**, *1*, 539–543.
[23] C. Sun, X. Yang, J. Chen, Z. Li, X. Lou, C. Li, S. Smith, G. Lu, H. Yang, *Chem. Commun.* **2010**, *46*, 6129–6131.
[24] J.Chen. , Y. Tan, Y. Cheah. D. Luan, S. Madhavi, F. Boey, L. Archer, X. Lou, *J. Am. Chem. Soc.* **2010**, *132*, 6124–6130.
[25] Z. Wang, Y. Zhang, T. Xia, J. Murowchick, G. Liu, X. Chen, *Energy Technology.* **2014**, *2*, 376–382.
[26] S. Ding, J. Chen, D. Luan, F. Boey, S. Madhavi, X. Lou, *Chem. Commun.* **2011**, *47*, 5780–5782.
[27] Z. Wang, J. Sha, E. Liu, C. He, C. Shi, J. Li, N. Zhao, *J. Mater. Chem. A.* **2014**, *2*, 8893–8901.
[28] H. Yang, C. Sun, S. Qiao, J. Zou, G. Liu, S. Smith, H. Cheng, G. Lu, *Nature.* **2008**, *453*, 638–641.
[29] X. Han, Q. Kuang, M. Jin, Z. Xie, L. Zheng, *J. Am. Chem. Soc.* **2009**, *131*, 3152–3153.
[30] G. Ma, Z. Wang, B. Gao, T. Ding, Q. Zhong, X. Peng, J. Su, B. Hu, L. Yuan, P. Chu, J. Zhou, K. Huo, *J. Mater. Chem. A.* **2015**, *3*, 14617–14624.
[31] X. Xiao, X. Peng, H. Jin, T. Li, C. Zhang, B. Gao, B. Hu, K. Huo, J. Zhou, *Adv. Mater.* **2013**, *25*, 5091–5097.
[32] B. Gao, X. Li, X. Guo, X. Zhang, X. Peng, L. Wang, J. Fu, P. Chu, Huo, *K. Adv. Mater. Interfaces.* **2015**, *2*, 1500211.
[33] N. Li, G. Zhou, R. Fang, F. Li, H. Cheng, *Nanoscale* **2013**, *5*, 7780–7784.
[34] F. Tian, Y, Zhang, J. Zhang, C. Pan, *J. Phys. Chem. C* **2012**, *116*, 7515–7519.
[35] V. Agubra, L Zuniga, D Flores, J Villareal, M Alcoutlabi, *Electrochimica Acta* **2016**, *192*, 529–550.
[36] L. Ji, Z. Lin, M. Alcoutlabi, X. Zhang, *Energy Environ. Sci.* **2011**, *4*, 2682–2699.
[37] V. Agubra, L. Zuniga, D. Garza, L. Gallegos, M. Pokhrel, M. Alcoutlabi, *Solid State Ion.* **2016**, *286*, 72–82.
[38] Y. Shi, L. Wen, F. Li, H. Cheng, *J. Power Sources.* **2011**, *196*, 8610–8617.
[39] G. Zhang, H. Wu, T. Song, U. Paik, X. Lou, *Angew. Chem. Int. Ed.* **2014**, *53*, 12590–12593.
[40] Y. Chen, X. Ma, X. Cui, Z. Jiang, *J. Power Sources.* **2016**, *302*, 233–239.
[41] H. Wu, X. Lou, H. Hng, *Chem. Eur. J.* **2012**, *18*, 2094–2099.
[42] J. Shin, D. Samuelis, J. Maier, *Adv. Funct. Mater.* **2011**, *21*, 3464–3472.
[43] X. Yang, Y. Yang, H. Hou, Y. Zhang, L. Fang, J. Chen, X. Ji, *J. Phys. Chem. C.* **2015**, *119*, 3923–3930.
[44] S. Chu, Y. Zhong, R. Cai, Z. Zhang, S. Wei, Z. Shao, *Small.* **2016**, *12*, 6724–6734.
[45] J. Ye, W. Liu, J. Cai, S. Chen, X. Zhao, H. Zhou, L. Qi, *J. Am. Chem. Soc.* **2011**, *133*, 933–940.
[46] B. Zhao, Z. Shao, *J. Phys. Chem. C.* **2012**, *116*, 17440–17447.
[47] X. Cheng, M. Hu, R. Huang, J. Jiang, *ACS Appl. Mater. Interfaces.* **2014**, *6*, 19176–19183.
[48] X. Liu, Z. Yang, F. Pan, L. Gu, Y. Yu, *Chem. Eur. J.* **2017**, *23.* 1757–1762
[49] L. Zhang, H. Li, Y. Ni, J. Li, K. Liao, G. Zhao, *Electrochem. Commun.* **2009**, *11*, 812–815.
[50] H. Kim, J. Lee, H. Ahn, O. Kim, M. Park, *Nat. Commun.* **2015**, *6*, 7278–7288.
[51] N. Kyeremateng, F. Vacandio, M. Sougrati, H. Martinez, J. Jumas, P. Knauth, T. Djenizian, *J. Power Sources* **2013**, *224*, 269–277.
[52] X. Peng, X. Zhang, L. Wang, L. Hu, S. Cheng, C. Huang, B. Gao, F. Ma, K. Huo, P. Chu, *Adv. Funct. Mater.* **2016**, *26*, 784–791.
[53] S. Xu, C. Hessel, H. Ren, R. Yu, Q. Jin, M. Yang, H. Zhao, D. Wang, *Energy Environ. Sci.* **2014**, *7*, 632–637.
[54] L. Ji, P. Meduri, V. Agubra, X. Xiao, M. Alcoutlabi, *Adv. Energy Mater.* **2016**, *6*, 1502159

Manuscript received: June 3, 2017
Version of record online: August 10, 2017